Large-Scale Micromagnetics Simulation of Magnetization Dynamics in a Permanent Magnet during the Initial Magnetization Process

Hiroshi Tsukahara,[1] Kaoru Iwano,[1] Tadashi Ishikawa,[1] Chiharu Mitsumata,[2] and Kanta Ono[1,*]

[1] *High Energy Accelerator Research Organization (KEK), Tsukuba, Ibaraki 305-0801, Japan*
[2] *National Institute for Materials Science (NIMS), Tsukuba 305-0047, Japan*

(Received 3 July 2018; revised manuscript received 4 September 2018; published 7 January 2019)

Large-scale micromagnetics simulations based on the Landau-Lifshitz-Gilbert equation are performed to clarify the initial magnetization process of a $Nd_2Fe_{14}B$ hot-deformed permanent magnet. A simulation model of the permanent magnet having 5302 grains is capable of elucidating the effects of networks among the grains. The calculated initial magnetization curve of the permanent magnet reproduces the two-step structure found in experiments. In the demagnetized state obtained from random magnetic configuration, multi- and single-magnetic-domain structures are formed in tabular grains that constitute the hot-deformed permanent magnet. The external magnetic field displaces the domain wall during the first step in the initial magnetization curve, and the multidomain grains disappear after the first step. In the second step, the magnetization reversal of the single domain occurs in grains with magnetization opposite the external field, and the magnetization reversal tends to occur in the grains with the easy axis tilted from the bulk easy magnetization axis. The average magnetic switching field of these single-domain grains is slightly higher than that of the bulk hot-deformed permanent magnet, and the domain-wall displacement across the grain boundary reduces the coercivity by 3.57 kOe in our simulation model. This discrepancy enables us to estimate the effects of networks among the grains through the dipolar interaction.

DOI: 10.1103/PhysRevApplied.11.014010

I. INTRODUCTION

Owing to the expected greatly increasing demand for electric vehicles in the near future, a high-performance permanent magnet, which is the most important material for motors, with minimal use of heavy rare-earth elements is being extensively developed [1]. Among the heavy-rare-earth-free high-performance permanent magnets, a hot-deformed permanent magnet is one of the most promising candidates with both high coercivity and remanent magnetization [2–5]. These hot-deformed permanent magnets consist of tabular grains with diameters of a few hundred nanometers. The coercivity is enhanced by the infiltration process that decreases magnetic interactions among the grains [6–8]. However, the high-coercivity mechanism for hot-deformed permanent magnets remains to be established, and it is important to clarify the effect of the intergrain interaction to design high-performance permanent magnets.

The distinct features of hot-deformed permanent magnets are that the initial magnetization curve has a two-step structure [9–13], unlike the single-step structure observed in conventional sintered permanent magnets. The two-step structure is enhanced by the improvement of the grain boundary, which also increases the coercivity of the hot-deformed permanent magnet. Hence, this two-step structure in the initial magnetization curve may be key to understanding the high-coercivity mechanism of hot-deformed permanent magnets, and it is also important to clarify the relationship between coercivity and the second step. Magnetization dynamics in permanent magnets has been investigated for many years [14] because the inhibition of domain-wall motion across grain boundaries is expected to affect the initial magnetization curve [15–21].

We need to investigate the motion of the magnetic domain wall in the magnet to clarify the two-step structure in the initial magnetization curve of a hot-deformed permanent magnet; however, direct experimental observation of the magnetization dynamics inside the permanent magnets is rather difficult. Instead, micromagnetics simulations are used to reveal the magnetization dynamics in permanent magnets [22–26]. Micromagnetics simulations enable the observation of the details of domain-wall motion and the complex magnetic interactions among the grains. For realistic micromagnetics simulations of permanent magnets, micrometer-sized simulation models discretized into nanometer-sized calculation cells must be used owing to the discrepancy between the sizes of the grains and the domain-wall width. Thus, large-scale micromagnetics simulations are indispensable for investigation

*kanta.ono@kek.jp

of magnetization dynamics within permanent magnets [27–29].

In this study, we perform a micromagnetics simulation with a large model with 5302 grains based on the Landau-Lifshitz-Gilbert equation to reveal the magnetization dynamics during the initial magnetization process of a hot-deformed permanent magnet. We investigate the demagnetized state under zero external field, in which multidomain and single-domain structures are formed. Then we calculate the initial magnetization curve, which shows a two-step structure, and we find that the grains tend to have a single-domain structure and that magnetization reversal is independent of the magnetization in the other grains in the second step. We estimate the effects of networks among the grains owing to the dipole field by comparison of results for the reversal of the field of the individual single-domain grains and the coercivity of the bulk permanent magnet.

II. MODEL AND METHOD

Figure 1(a) shows a three-dimensional image of the simulation model for a hot-deformed permanent magnet. The simulation model with a size of $2048 \times 2048 \times 512$ nm^3 is constructed by our stacking layers that consist of tabular grains with thickness of 32 nm. These layers are created by the following procedure. First, we randomly place circles in the two-dimensional system with periodic boundary conditions. Repulsive forces act between the circles, the diameters of which have a Gaussian distribution. The repulsive force potential of the ith circle is written as $U_i = \sum_j A_p \exp\{-[d_{ij} - (r_i + r_j)]/r_d\}$, where A_p is a constant, r_d is the decay radius, and d_{ij} is the distance between the ith circle and the jth circle, whose radii are r_i and r_j, respectively [30]. We assume $A_p = 2.0$ J and $r_d = 5.0$ nm. After calculating the dynamics of the circles using the conventional molecular-dynamics technique, we obtain equilibrium positions for the center of each circle. Finally, the layers for the simulation model are created by our dividing the two-dimensional system using a Voronoi tessellation created from the positions of the circle centers. We tilt the easy axis of each grain, $\hat{\mathbf{e}}_a(\mathbf{x})$, from the z axis as shown in Fig. 1(b). The tilt angle of the easy axis, $\Delta\theta$, is set to have a von Mises distribution, and the azimuth angle, ϕ, is randomly distributed. Figure 1(c) shows the distribution of the diameter of individual grains and $\Delta\theta$ of the simulation model. To estimate the diameter of an individual grain, we assume the shape of the grain is cylindrical. Thus, the grain diameter is defined as $\sqrt{V/\pi d}$, where V is the volume of the grain and d is the thickness of the grain. In total, 5302 grains are used in this model. The grain diameter ranges from 98.2 to 154.8 nm, and the average diameter is 126.7 nm. The average $\Delta\theta$ is 11.5°, and the maximum angle is 55.3°.

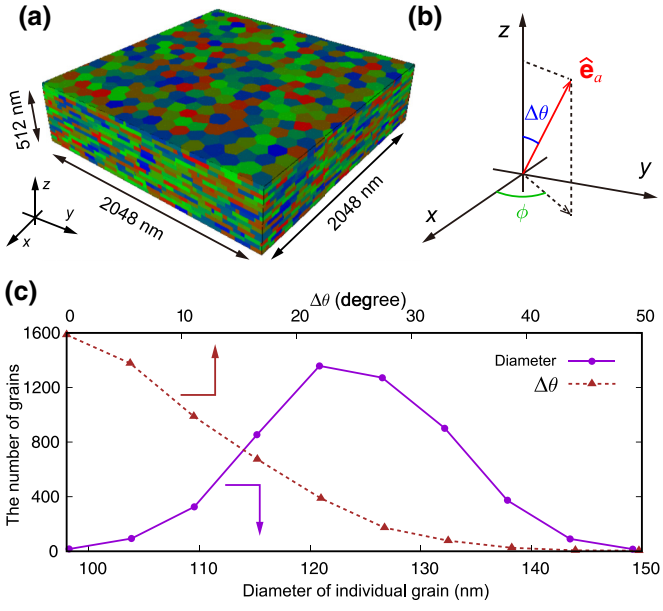

FIG. 1. (a) Simulation model for the hot-deformed permanent magnet (the color indicates each tabular-grain region). (b) Definitions of the tilt angle, $\Delta\theta$, from the z axis and the azimuth angle, ϕ, of the easy axis, $\hat{\mathbf{e}}_a(\mathbf{x})$. (c) Distributions of the grain diameter and $\Delta\theta$. The solid line (dotted line) and circles (triangles) represent the number of grains as a function of the diameter of an individual grain ($\Delta\theta$).

We perform the micromagnetics simulation using the simulation model shown in Fig. 1(a). Magnetization dynamics is calculated by our solving the Landau-Lifshitz-Gilbert equation, which is

$$\frac{d\mathbf{m}(\mathbf{x})}{dt} = -\gamma\mathbf{m}(\mathbf{x}) \times \mathbf{H}_{\text{eff}}(\mathbf{x}) + \alpha\mathbf{m}(\mathbf{x}) \times \frac{d\mathbf{m}(\mathbf{x})}{dt}, \quad (1)$$

where $\mathbf{x}$ is a position vector, $\mathbf{m}(\mathbf{x})$ is the normalized magnetization, α is the Gilbert damping constant, γ is the gyromagnetic ratio, and $\mathbf{H}_{\text{eff}}(\mathbf{x}) = \delta w/\delta\mathbf{m}$ is the effective field. We assume that the magnetic Gibbs-free-energy density, w, consists of external, $w_{\text{ext}} = -M_s\mathbf{m} \cdot \mathbf{H}_{\text{ext}}$, dipolar, $w_{\text{dip}} = -0.5M_s\mathbf{m} \cdot \mathbf{H}_{\text{dip}}$, exchange, w_{exc}, and anisotropic, w_{ani}, energy densities, where

$$w_{\text{exc}} = A(\mathbf{x})[|\nabla m_x(\mathbf{x})|^2 + |\nabla m_y(\mathbf{x})|^2 + |\nabla m_z(\mathbf{x})|^2], \quad (2)$$

$$w_{\text{ani}} = K_{1u}\{1 - [\mathbf{m} \cdot \hat{\mathbf{e}}_a(\mathbf{x})]^2\}, \quad (3)$$

where $A(\mathbf{x})$ is the exchange-stiffness constant and K_{1u} is the uniaxial-anisotropy constant, M_s is the saturation magnetization, $\mathbf{H}_{\text{ext}}$ is the external field, and $\mathbf{H}_{\text{dip}}$ is the dipole field [31–33]. The dipole field is calculated with fast Fourier transform, which reducesthe calculation time for this field to $O(n\log n)$, where n is the number of calculation cells. We calculate the time development of the magnetization using the Runge-Kutta-Fehlberg method with an adjustable time step [34]. The development of magnetization and an error are calculated by fourth- and fifth-order

Runge-Kutta method, respectively (RKF45). We set the accuracy to 1.0×10^{-4}, and the safety factor to 0.95 for RKF45. The magnetization is considered to have converged after the magnitude of the averaged torque reaches 1.0×10^{-3} s^{-1}.

We segment the simulation model into 268 435 456 cubic cells with dimensions $2.0 \times 2.0 \times 2.0$ nm^3 and calculate the magnetization dynamics using the finite-difference method under periodic boundary conditions to investigate the magnetization dynamics in the permanent magnet. We select the following $Nd_2Fe_{14}B$ material parameters [35–40]: $M_s = 1281.2$ emu/cm^3, $K_{1u} = 4.5 \times 10^7$ erg/cm^3, $\alpha = 1.0$, and $|\gamma| = 1.76 \times 10^7$ s^{-1} G^{-1}. We set the exchange-stiffness constant, $A(\mathbf{x})$, to 12.5×10^{-7} erg/cm for intragrain exchange interactions. We consider the thinnest limit of the grain-boundary phase. In previous work, we performed the simulation with the exchange-stiffness constant set to 12.5×10^{-9} erg/cm between the grain and the grain-boundary phase, and we obtained demagnetization curves with shapes in good agreement with the experimental results [41]. Hence, we set the same-exchange stiffness constant for intergrain exchange interactions to include the effects of the thin grain-boundary phase. We do not consider defects in the simulation model. The micromagnetic simulation is performed on Blue Gene/Q at KEK in Japan with use of our simulator [42–44].

The simulation is executed by our performing the following procedure. First, we orient the magnetization of each cell completely at random to form an initial magnetization state. We then calculate the magnetization dynamics under no external field to obtain a demagnetized state under zero external field. After obtaining this state, we apply the external field along the $+z$ direction and calculate the stable magnetization state. In addition, we perform micromagnetics simulation using another simulation model whose averaged diameter and $\Delta\theta$ are almost the same, and the initial magnetization curve of this simulation model also has a two-step structure. Hence, the properties of the magnetization dynamics during the initial magnetization process are independent of the initial seed for a pseudorandom number in our large-scale simulation.

After performing the simulation, we calculate the magnetic correlation function for m_z, which is defined as

$$C_{zz}(\mathbf{r}) = \frac{1}{\Omega}\int d\mathbf{x} m_z(\mathbf{x}) m_z(\mathbf{x}+\mathbf{r}), \tag{4}$$

where Ω is the volume of the simulation model and $\mathbf{r}$ is the distance between the two points. We integrate over the entire simulation model. The magnetic correlation function becomes constant when the magnetization distribution is uniform, and the magnetic correlation function oscillates when the magnetic configuration is periodic. According to Kronmüller [20], the coercivity of an uncorrelated permanent magnet is

$$\langle H_c^{\mathrm{nc}}\rangle_{\mathrm{avg}} = \frac{2K_{1u}}{M_s}\langle \alpha_K \alpha_\psi \rangle_{\mathrm{avg}} - N_{\mathrm{eff}} M_s, \tag{5}$$

where $\langle \alpha_K \alpha_\psi \rangle_{\mathrm{avg}}$ is the averaged structural reduction factor and N_{eff} is the effective demagnetization factor. In the demagnetization process, the domain wall moves across the grain boundary owing to the dipole field [29]. The real permanent magnet has a network among the grains owing to the intergrain interactions. If the intergrain interaction consists of only a dipole field, and we assume that N_{eff} inside the grain is unchanged throughout the initial magnetization and demagnetization processes, the coercivity of the permanent magnet can be written as

$$H_c = \langle H_c^{\mathrm{nc}}\rangle_{\mathrm{avg}} - N_{\mathrm{eff}}^D M_s, \tag{6}$$

where the correction factor N_{eff}^D represents the effects of the domain-wall displacement across the grain boundary on the coercivity due to the dipole field.

III. RESULTS AND DISCUSSION

A. Demagnetized state under zero external field

Figure 2(a) shows a three-dimensional magnetization-distribution image of the calculated demagnetized state under zero external field. The magnetization distribution in the magnet shows a complex magnetic domain structure owing to the interplay between the exchange interaction and the dipolar interaction. The magnetization configuration of the demagnetized state is completely different from that of the demagnetization process, where an interaction domain structure appears [29]. A mazelike domain is observed in the xy plane, whereas in the z direction, the magnetization tends to be aligned to form a columnar structure because of the dipolar interaction.

Figure 2(b) shows a cross section of the magnetization distribution of m_z in the xy plane at $z = 16$ nm. The mazelike complex magnetic domain structure in the xy plane consist of single-domain and multidomain grains. The magnetic domain structure has domain walls at the boundary of the magnetic domain, and the energy of the domain wall is described by $4\sqrt{A(\mathbf{x})K_{1u}(\mathbf{x})}$, where $A(\mathbf{x})$ and $K_{1u}(\mathbf{x})$ are the exchange-stiffness and uniaxial-anisotropy constants at $\mathbf{x}$, respectively [45–48]. Hence, the energy of the domain wall is minimized when the magnetic domain walls are placed on the grain boundary, where the exchange-stiffness constant is smaller than inside the grain. However, as mentioned above, the columnar structure tends to be created by the dipolar interaction along the z direction, and the grains have an overlapping region between them. Thus, the domain walls of the mazelike

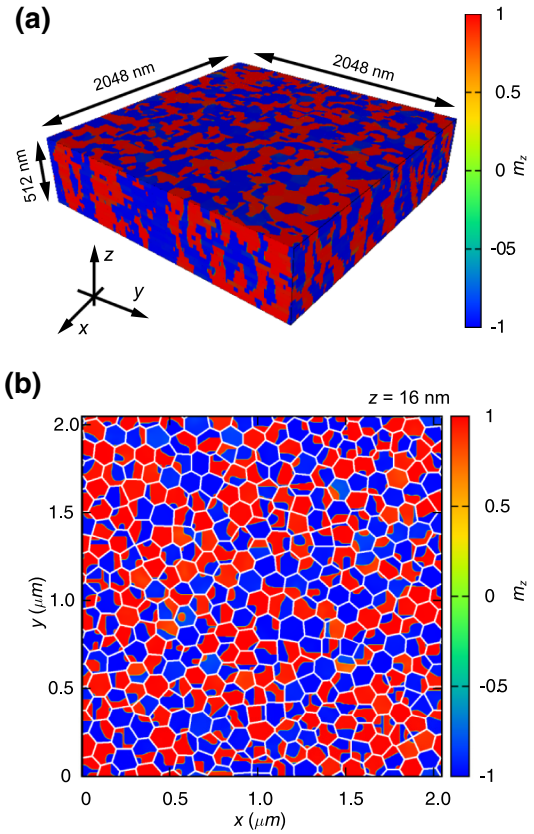

FIG. 2. (a) Three-dimensional magnetization-distribution image of the demagnetized state under zero external field (the color represents the value of m_z). (b) A cross section of the demagnetized state in the xy plane at $z = 16$ nm (white lines indicate the grain boundaries).

magnetic domain are placed inside the grain and at the grain boundary. This complex domain structure results in various modes of magnetization reversal in an initial magnetization process of the hot-deformed permanent magnet.

B. Demagnetization process

A demagnetization curve of this simulation model is shown in Fig. 3(a). The magnetization reversal is nucleated. When the external field approaches the coercive field, nucleation cores are created around a corner of grains whose $\Delta\theta$ tends to be larger than that of other grains. A local strong dipole field is another important feature for the occurrence of the nucleation core. The dipole field is not uniform inside the permanent magnet owing to the random misorientation of the easy axis. In some region, a dipole field exceeding 1.0 T is applied to the grain along the $-z$ direction. When the strong dipole field is applied to the corner of the grain, the nucleation core tends to be created. Afterward, magnetization-reversal regions expand among the grains. Hence, the dipolar interaction plays an important role in magnetization-reversal processes. The coercivity of this model is 29.94 kOe.

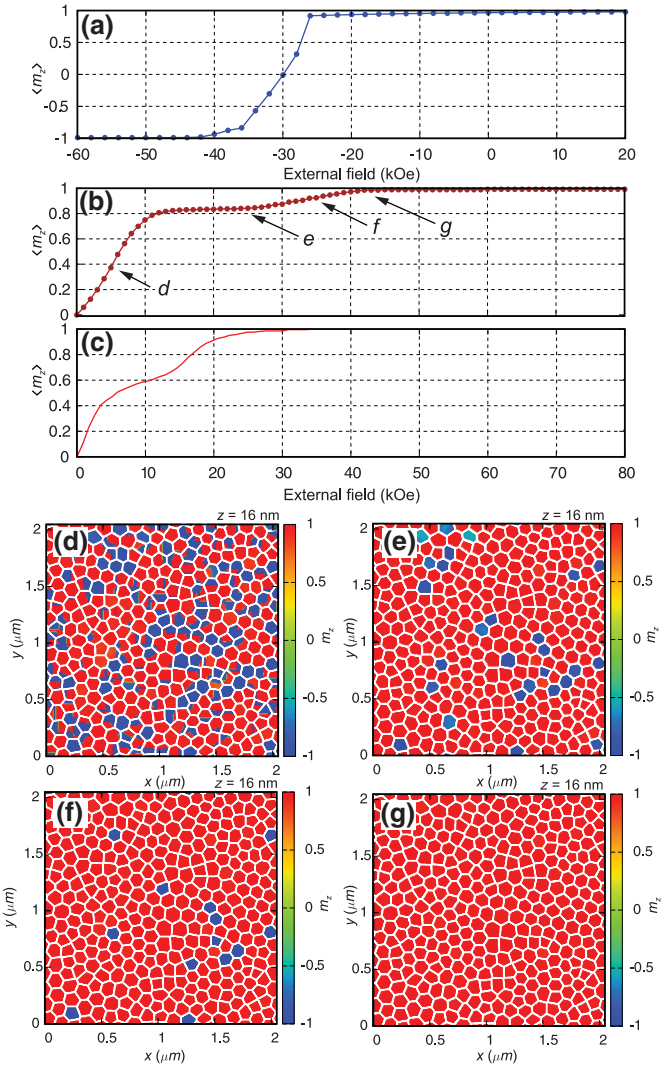

FIG. 3. (a) Calculated demagnetization curve, (b) calculated initial magnetization curve, and (c) experimental initial magnetization curve [10]. Cross section of the magnetization distribution at various external magnetic fields H_{ext}: (d) 5 kOe, (e) 25 kOe, (f) 35 kOe, and (g) 42 kOe.

C. Initial magnetization process

Figure 3(b) shows the calculated initial magnetization and demagnetization curves from the micromagnetics simulation. The initial magnetization curve has the two-step structure that has been observed in experiments as shown in Fig. 3(c) [10–14]. When the external field is less than 13.0 kOe, the average m_z quickly increases as the external field increases. Subsequently, the initial magnetization curve is constant until the external field exceeds 25.0 kOe. The average m_z increases again when the external field is between 26.0 and 42.0 kOe, and the simulation model is magnetized after the external field exceeds 43.0 kOe.

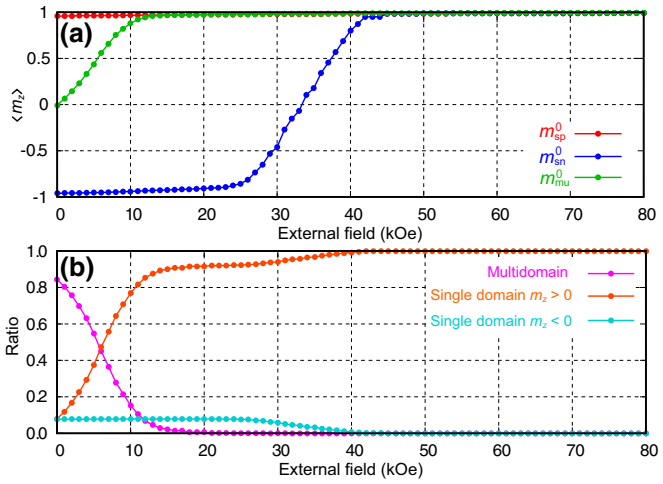

FIG. 4. (a) Magnetization curves for $m^0_{\rm mu}$ (green), $m^0_{\rm sp}$ (red), and $m^0_{\rm sn}$ (blue) as a function of the external field. (b) Ratio of the number of grains with the multidomain structure (magenta) and single-domain structures with positive m_z (orange) and negative m_z (cyan) as a function of the external field.

We calculate $\langle H_c^{\rm nc}\rangle_{\rm avg}$ using the magnetization-reversal field and $\Delta\theta$ of the grains in which the magnetization is revered during the second step of the initial magnetization curve. In our simulation, $\langle H_c^{\rm nc}\rangle_{\rm avg}$ is 33.51 kOe, which is larger than the coercivity of this model, and $N^D_{\rm eff}$ in Eq. (6) is estimated as 0.222. If the magnetization is reversed independently inside the grains, the discrepancy represents the effects of networks among the grains.

To investigate the domain-wall motion in the hot-deformed permanent magnet, the cross sections of the magnetization distribution at some external field are shown in Figs. 3(d)–3(g), and the magnetization curves of grains according to the multidomain structure ($m^0_{\rm mu}$) and single-domain structures with positive m_z ($m^0_{\rm sp}$) and negative m_z ($m^0_{\rm sn}$) in the demagnetized state under zero external field are shown in Fig. 4(a). In the first step [Fig. 3(d): $H_{\rm ext} = 5$ kOe], compared with Fig. 2, the domain walls move into the multidomain grains. Hence, only $m^0_{\rm mu}$ increases, and $m^0_{\rm sp}$ and $m^0_{\rm sn}$ are constant in this step. Afterward, the motion of the domain wall stops at the grain boundaries because the exchange fields are small at the interfaces between grains. The average m_z is insensitive to the increase in the external field up to $H_{\rm ext} = 25$ kOe, and all grains have a single-domain structure at $H_{\rm ext} = 25$ kOe, as shown in Fig. 3(e). In the second step [Fig. 3(f): $H_{\rm ext} = 35$ kOe], the magnetization reverses in the single-domain grains with negative m_z, as shown by the magnetization curve of $m^0_{\rm sn}$ in Fig. 4(a). Finally, all grains are magnetized as shown in Fig. 3(g). As shown in our previous work [49], the coercivity decreases with increasing intergrain interaction due to the displacement of the domain wall across the grain boundaries. As the intergrain exchange interaction increases, it is expected that the domain-wall displacement between the grains occurs in the initial magnetization process and the two-step structure disappears.

The behavior of the domain-wall motion is also investigated by the number of multidomain and single-domain grains, as shown in Fig. 4(b). In the first step, the number of multidomain grains decreases, and the number of single-domain grains with positive m_z increases owing to the motion of the domain wall toward the grain boundary. Multidomain grains cease to exist at $m_z > 20$ kOe. In contrast, the number of single-domain grains with negative m_z is constant until the second step in the initial magnetization curve. In the second step, the magnetization reverses in single-domain grains with negative m_z and the number of single-domain grains with positive m_z increases.

The magnetic correlation function is an autocorrelation function of magnetization distribution, and it represents the magnetic configuration of magnetic materials. The domain-wall displacement and the stoppage of the domain-wall motion at the grain boundary are clarified by the correlation function for m_z. When the magnetization distribution is uniform, the magnetic correlation function for m_z should be constant. In contrast, the magnetic correlation function oscillates when the magnetization distribution is periodic. Figure 5 shows the magnetic correlation function for m_z as a function of r_x and r_z, which represent the distances of two points along the x direction and the z direction, respectively, under various external fields. In the case of the demagnetized state ($H_{\rm ext} = 0$ kOe), the magnetic correlation function in the x direction quickly attenuates while slightly oscillating, and it becomes zero at $r_x \geq 200$ nm. In the z direction, the attenuation ratioof

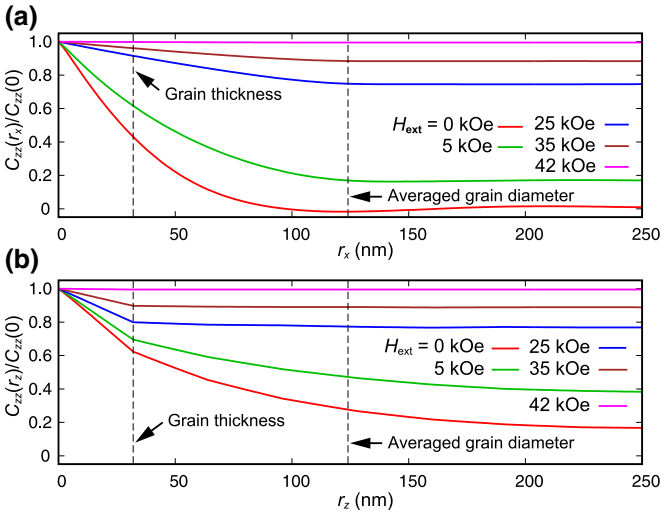

FIG. 5. Magnetic correlation function for m_z along (a) the x direction and (b) the z direction at various external fields: 0.0 kOe (red), 5.0 kOe (green), 25.0 kOe (blue), 35.0 kOe (brown), and 42 kOe (purple).

the magnetic correlation function is smaller than that in the x direction, and the correlation function has a finite value even at $r_x = 250$ nm. Hence, it is revealed quantitatively that the demagnetized state has a columnar structure and a mazelike magnetic domain along the z direction and in the xy plane (see Fig. 2). As the external field increases, the attenuation ratios become small in both the x direction and the z direction because regions with positive m_z are expanded by the displacements of the domain wall. At the beginning of the second step in the initial magnetization curve ($H_{\rm ext} = 25$ kOe), the autocorrelation functions become flat in both the x direction and the z direction after r_x and r_z exceed the grain thickness (32 nm) and the averaged grain diameter (126.7 nm), respectively. These behaviors indicate that grains that have a single-domain structure with negative m_z tend to be isolated from each other. After the external field exceeds the value at the end of the second step ($H_{\rm ext} = 35$ kOe), the correlation functions are constant at all r_x and r_z because the magnetization process is complete.

The magnetization reversal of grains with negative m_z independently occurs in the second step, and we can evaluate the reversal field of the grains as the external field $H_1^{\rm sd}$, where the magnetization of the single-domain grains with negative m_z is reversed. We also evaluate the external field $H_1^{\rm mu}$, where m_z of the multidomain grain is 0.5 in the first step. Figure 6 shows the dependence of $H_1^{\rm sd}$ and $H_1^{\rm mu}$ as a function of the diameter of an individual grain and $\Delta\theta$. $H_1^{\rm mu}$ shows no correlation to the diameter of an individual grain and $\Delta\theta$, indicating the domain-wall displacement inside the grain does not depend on the grain diameter and $\Delta\theta$. In contrast, $H_1^{\rm sd}$ correlates to $\Delta\theta$. Magnetization reversal of the grain with large $\Delta\theta$ occurs easily. $H_1^{\rm sd}$ shows a small correlation to the diameter of an individual grain as shown in previous studies [50–52]. The average $H_1^{\rm sd}$ is identical to the coercivity of a permanent magnet that consists of uncorrelated grains because the magnetization of a grain with negative m_z is independently reversed.

Estimation of the effect of the intergrain interaction is difficult with only the demagnetization curve because the domain wall moves across the grain boundary during the demagnetization process [29]. In contrast, the magnetization is individually reversed inside the grains in the second step in the initial magnetization curve. Our simulation indicates that the discrepancy between the coercivity and $\langle H_c^{\rm nc}\rangle_{\rm avg}$ enables estimation of the strength of the intergrain interaction that reduces the coercivity. In this study, the dipole field governs the intergrain interaction because the exchange constant is small at the grain boundary. Thus, we can use Eq. (6) and estimate the corrective factor $N_{\rm eff}^D$.

To design a high-coercivity magnet, it is desirable to reduce $N_{\rm eff}^D$, which represents the coupling among the grains owing to the dipole field. $N_{\rm eff}^D$ relates to textures of the permanent magnet. The nucleation cores are created at the corner of the grain around which the strong dipole field is locally applied during the demagnetization process. Hence, the reduction of the network of the dipole field by change of the texture of the permanent magnet leads to a design for new high-performance permanent magnets. In future work, we will perform micromagnetics simulation during the demagnetization process while changing the shape of the grain, the distribution of $\Delta\theta$, and the grain-boundary phase to improve the performance of the permanent magnet.

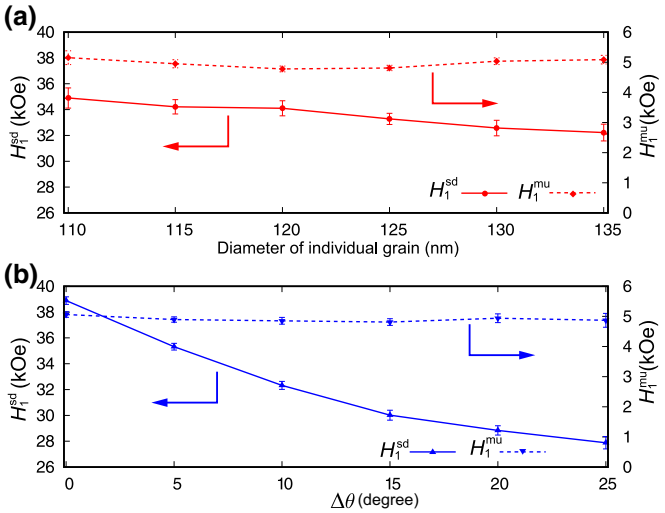

FIG. 6. Reversal field of the grains $H_1^{\rm sd}$ (external field where the magnetization is reversed within the single-domain grains with negative m_z in the second step), and the field $H_1^{\rm mu}$ under which m_z of the multidomain grain becomes 0.5 in the first step, as a function of (a) the diameter of an individual grain and (b) $\Delta\theta$.

IV. SUMMARY

We clarify the demagnetized state under zero external field and the magnetization dynamics during the initial magnetization process of a hot-deformed permanent magnet by performing a large-scale micromagnetics simulation that consists of 5302 tabular grains. In the demagnetized state, mazelike domains appear in the xy plane. In contrast, the magnetization tends to form a columnar structure in the z direction owing to the dipolar interaction. The mazelike structure is created by the multidomain structure and single-domain structures with positive or negative m_z that formed spontaneously owing to the interplay between the exchange interaction and the dipolar interaction.

Starting from the demagnetized state, we simulate the magnetization dynamics during the initial magnetization process by applying an external field. The calculated initial magnetization curve has the two-step structure that was observed in experiments. In the first step, the domain walls in the multidomain grains move to the grain boundaries, and the number of single-domain grains with positive m_z increases; however, the number of single-domain grains

with negative m_z is constant during the first step. The magnetization of individual single-domain grains with negative m_z reverses in the second step

The magnetization reversal within individual grains enables us to estimate the effects of the domain-wall displacement across the grain boundary on the coercivity of the permanent magnet. In our simulation, the averaged switching field of the individual grains is larger than the coercivity of the simulation model with networks among the grains. If the effective demagnetization factor of the grain is unchanged throughout the initial magnetization and demagnetization processes, the difference between the coercivities of the former and the latter represents the effect of the domain-wall motion across the grain boundary owing to the dipolar interaction.

ACKNOWLEDGMENT

This work is partly supported by the Elements Strategy Initiative Center for Magnetic Materials (ESICMM) under the outsourcing project of the Ministry of Education, Culture, Sports, Science, Technology (MEXT). We gratefully acknowledge the financial support by Toyota Motor Corporation. The supercomputer simulations were performed by the Large Scale Simulation Program 15/16-18 of the High Energy Accelerator Research Organization (KEK). The authors would like to express their sincere thanks to the crew of Center for Computational Materials Science of the Institute for Materials Research, Tohoku University for their continuous support of the supercomputing facilities.

[1] O. Gutfleisch, M. A. Willard, E. Brück, C. H. Chen, S. G. Sankar, and J. P. Liu, Magnetic materials and devices for the 21st century: Stronger, lighter, and more energy efficient, Adv. Mater. **23**, 821 (2011).

[2] R. W. Lee, Hot-pressed neodymium-iron-boron magnets, Appl. Phys. Lett. **46**, 790 (1985).

[3] R. W. Lee, E. G. Brewer, and N. A. Schaffel, Processing of Neodymium-Iron-Boron melt-spun ribbons to fully dense magnets, IEEE Trans. Magn. **21**, 1958 (1985).

[4] R. K. Mishra, and R. W. Lee, Microstructure, domain walls, and magnetization reversal in hot-pressed Nd-Fe-B magnets, Appl. Phys. Lett. **48**, 733 (1986).

[5] R. K. Mishra, T.-Yao Chu, and L. K. Rabenberg, The development of the microstructure of die-upset Nd-Fe-B magnets, J. Magn. Magn. Mater. **84**, 88 (1990).

[6] L. Liu, H. Sepehri-Amin, T. Ohkubo, M. Yano, A. Kato, T. Shoji, and K. Hono, Coercivity enhancement of hot-deformed Nd-Fe-B magnets by the eutectic grain boundary diffusion process, J. Alloy. Comp. **666**, 432 (2016).

[7] U. M. R. Seelam, L. Liu, T. Akiya, H. Sepehri-Amin, T. Ohkubo, N. Sakuma, M. Yano, A. Kato, and K. Hono, Coercivity of the Nd-Fe-B hot-deformed magnets diffusion-processed with low melting temperature glass forming alloys, J. Magn. Magn. Mater. **412**, 234 (2016).

[8] L. Liu, H. Sepehri-Amin, T. Ohkubo, M. Yano, A. Kato, N. Sakuma, T. Shoji, and K. Hono, Coercivity enhancement of hot-deformed Nd-Fe-B magnets by the eutectic grain boundary diffusion process using Nd 62 Dy 20 Al 18 alloy, Scr. Mater. **129**, 44 (2017).

[9] F. E. Pinkerton, and D. J. Van Wingerden, Magnetization process in rapidly solidified neodymium-iron-boron permanent magnet materials, J. Appl. Phys. **60**, 3685 (1986).

[10] S. Sawatzki, I. Dirba, L. Schultz, and O. Gutfleisch, Electrical and magnetic properties of hot-deformed Nd-Fe-B magnets with different DyF3 additions, J. Appl. Phys. **114**, 133902 (2013).

[11] K. Hioki, A. Hattori, and T. Iriyama, Development of Dy-free hot-deformed Nd-Fe-B magnets by optimizing chemical composition and microstructure, J. Magn. Soc. Jpn. **38**, 79 (2014).

[12] T. Zhang, F. Chen, J. Wang, L. Zhang, Z. Zou, Z. Wang, F. Lu, and B. Hu, Improvement of magnetic performance of hot-deformed Nd-Fe-B magnets by secondary deformation process after Nd-Cu eutectic diffusion, Acta. Mater. **118**, 374 (2016).

[13] T. Zhang, F. Chen, T. Zheng, H. Wen, L. Zhang, and L. Zhou, Anisotropic behavior of grain boundary diffusion in hot-deformed Nd-Fe-B magnet, Scr. Mater. **129**, 1 (2017).

[14] M. Grönefeld, and H. Kronüller, Initial magnetization curve and hardening mechanism in rapidly quenched Nd-Fe-B magnets, J. Magn. Magn. Mater. **88**, L267 (1990).

[15] A. Menth, H. Nagel, and R. S. Perkins, New high-performance permanent magnets based on rare earth-transition metal compounds, Annu. Rev. Mater. Sci. **8**, 21 (1978).

[16] K.-D. Drust, and H. Kuronmüller, The coercive field of sintered and melt-spun NdFeB magnets, J. Magn. Magn. Mater. **68**, 63 (1987).

[17] G. C. Hadjipanayis, and J. Kim, Domain wall pinning versus nucleation of reversed domains in R-Fe-B magnets (invited), Appl. Phys. **63**, 3310 (1988).

[18] R. Friedberg, and D. I. Paul, New Theory of Coercive Force of Ferromagnetic Materials, Phys. Rev. Lett. **34**, 1234 (1975).

[19] H.-R. Hilzinger, and H. Kronmüller, Investigation of bloch-wall-pinning by antiphase boundaries in RCo5-compounds, Phys. Lett. A **51**, 59 (1975).

[20] H. Kronmüller, K.-D. Durst, and M. Sagawa, Analysis of the magnetic hardening mechanism in RE-FeB permanent magnets, J. Magn. Magn. Mater. **74**, 291 (1988).

[21] H. Kronmüller, and D. Goll, Micromagnetic theory of the pinning of domain walls at phase boundaries, Phys. B **319**, 122 (2002).

[22] T. Schrefl, J. Fidler, and H. Kronmüller, Remanence and coercivity in isotropic nanocrystalline permanent magnets, Phys. Rev. B **49**, 6100 (1994).

[23] R. Fischer, T. Schrefl, H. Kronmüller, and J. Fidler, Grain-size dependence of remanence and coercive field of isotropic nanocrystalline composite permanent magnets, J. Magn. Magn. Mater. **153**, 35 (1996).

[24] W. Rave, and K. Ramstöck, Micromagnetic calculation of the grain size dependence of remanence and coercivity in nanocrystalline permanent magnets, J. Magn. Magn. Mater. **171**, 69 (1997).

[25] J. Fidler, and T. Schrefl, Micromagnetic modelling – the current state of the art, J. Phys. D: Appl. Phys. **33**, R135 (2000).
[26] S.-J. Lee, S. Sato, H. Yanagihara, E. Kita, and C. Mitsumata, Numerical simulation of random magnetic anisotropy with solid magnetization grains, J. Magn. Magn. Mater. **323**, 28 (2011).
[27] J. Fujisaki, A. Furuya, Y. Uehara, K. Shimizu, H. Oshima, T. Ohkubo, S. Hirosawa, and K. Hono, Micromagnetic simulations of magnetization reversal in misaligned multi-grain magnets with various grain boundary properties using large-scale parallel computing, IEEE Trans. Magn. **50**, 7100704 (2014).
[28] H. Tsukahara, K. Iwano, C. Mitsumata, T. Ishikawa, and K. Ono, Magnetization reversal processes of isotropic permanent magnets with various inter-grain exchange interactions, AIP Adv. **7**, 056224 (2017).
[29] H. Tsukahara, K. Iwano, C. Mitsumata, T. Ishikawa, and K. Ono, Micromagnetic simulation for the magnetization reversal process of Nd-Fe-B hot-deformed nanocrystalline permanent magnets, AIP Adv. **7**, 056234 (2017).
[30] S. Erokhin, D. Berkov, N. Gorn, and A. Michels, Micromagnetic modeling and small-angle neutron scattering characterization of magnetic nanocomposites, Phy. Rev. B **85**, 024410 (2012).
[31] D. V. Berkov, and N. L. Gorn, *Handbook of Advanced Magnetic Materials* (Springer, New York, 2006), Vol. 2, p. 794.
[32] Y. Nakatani, Y. Uesaka, and N. Hayashi, Direct solution of the Landau-Lifshitz-Gilbert equation for micromagnetics, Jpn. J. Appl. Phys. **28**, 2485 (1989).
[33] H. Fukushima, Y. Nakatani, and N. Hayashi, Volume average demagnetizing tensor of rectangular prisms, IEEE Trans. Magn. **34**, 193 (1998).
[34] E. Fehlberg, NASA Technical Report R-315, 1969.
[35] J. J. Croat, J. F. Herbst, R. W. Lee, and F. E. Pinkerton, High-energy product Nd-Fe-B permanent magnets, Appl. Phys. Lett. **44**, 149 (1984).
[36] J. J. Croat, J. F. Herbst, R. W. Lee, and F. E. Pinkerton, Pr-Fe and Nd-Fe-based materials: A new class of high-performance permanent magnets (invited), J. Appl. Phys. **55**, 2078 (1984).
[37] M. Sagawa, S. Fujimura, N. Togawa, H. Yamamoto, and Y. Matsuura, New material for permanent magnets on a base of Nd and Fe (invited), J. Appl. Phys. **55**, 2083 (1984).
[38] M. Okuda, S. Sugimoto, C. Ishizaka, T. Tanaka, and M. Homma, Didymium-Fe-B sintered permanent magnets, J. Appl. Phys. **57**, 4146 (1985).
[39] M. Sagawa, S. Fujimura, H. Yamamoto, Y. Matsuura, and S. Hirosawa, Magnetic properties of rare-earth-iron-boron permanent magnet materials, J. Appl. **57**, 4094 (1985).
[40] T. Schrefl, and J. Fidler, Micromagnetic simulation of magnetizability of nanocomposite Nd-Fe-B magnets, J. Appl. Phys. **83**, 6262 (1998).
[41] H. Tsukahara, K. Iwano, C. Mitsumata, T. Ishikawa, and K. Ono, Effect of grain boundary phase on the magnetization reversal process of nanocrystalline magnet using large-scale micromagnetic simulation, AIP Adv. **8**, 056226 (2018).
[42] N. Inami, Y. Takeichi, C. Mitsumata, K. Iwano, T. Ishikawa, S.-J. Lee, H. Yanagihara, E. Kita, and K. Ono, IEEE Trans. Magn. **50**, 1400304 (2013).
[43] H. Tsukahara, S.-J. Lee, K. Iwano, N. Inami, T. Ishikawa, C. Mitsumata, H. Yanagihara, E. Kita, and K. Ono, Large-scale micromagnetics simulations with dipolar interaction using all-to-all communications, AIP Adv. **6**, 056405 (2016).
[44] H. Tsukahara, K. Iwano, C. Mitsumata, T. Ishikawa, and K. Ono, Implementation of low communication frequency 3D FFT algorithm for ultra-large-scale micromagnetics simulation, Comput. Phys. Commun. **207**, 217 (2016).
[45] C. Kittel, Physical theory of ferromagnetic domains, Rev. Mod. Phys. **21**, 541 (1949).
[46] B. A. Lilly, LXXI. Energies and widths of domain boundaries in ferromagnetics, Philos. Mag. **41**, 792 (1950).
[47] H. Kronmüller, and M. Fähnle, *Micromagnetism and the Microstructure of Ferromagnetic Solids* (Cambridge University Press, Cambridge, 2003), p. 51.
[48] A. Hubert, and R. Schäfer, *Magnetic Domains: The Analysis of Magnetic Microstructures.* (Springer, Berlin, Heidelberg, 1998), p. 201.
[49] H. Tsukahara, K. Iwano, C. Mitsumata, T. Ishikawa, and K. Ono, Magnetization reversal processes of isotropic permanent magnets with various inter-grain exchange interactions, AIP Adv. **7**, 056224 (2017).
[50] R. Fischer, and H. Kronmüller, Static computational micromagnetism of demagnetization processes in nanoscaled permanent magnets, Phys. Rev. B **54**, 7284 (1996).
[51] D. Goll, and H. Kronüller, High-performance permanent magnets, Naturwissen **87**, 423 (2000).
[52] S. Bance, B. Seebacher, T. Schrefl, L. Exl, M. Winklhofer, G. Hrkac, G. Zimanyi, T. Shoji, M. Yano, N. Sakuma, M. Ito, A. Kato, and A. Manabe, Grain-size dependent demagnetizing factors in permanent magnets, J. Appl. Phys. **116**, 233903 (2014).